Virtual Inertia from Smart Loads

Tong Chen, *Student Member, IEEE*, Jinrui Guo, *Student Member, IEEE*,
Balarko Chaudhuri, *Senior Member, IEEE* and Ron. S.Y. Hui, *Fellow, IEEE*

***Abstract*—The inertia of future power systems is expected to decrease with increasing penetration of renewable energy resources. Sufficient inertia is required to avoid large fluctuations in grid frequency and also limit the excessive rate of change of frequency (RoCoF). Unlike many previous works focusing on virtual inertia on the power supply side, this paper studies and quantifies potential virtual inertia from the load side. The analysis shows that, voltage-dependent loads coupled with electric spring (ES) technology can be operated as smart loads (SL) within the +/- 5% tolerance of the ac mains voltage and offer virtual inertia. Following the U.K. National Grid frequency requirements, it is shown that the ES based SL can provide virtual inertia up to an inertia coefficient of H_{SL}=2.5 s (when n_p=2) with respect to its load power rating. The effectiveness of such virtual inertia extraction from SL has been verified by the simulation study on a CIGRE benchmark microgrid with high-resolution domestic demand model. The value of H_{SL} is shown to be around 1.3 s during the most part of the day and can increase the overall system inertia coefficient by 0.53 s if all the domestic loads are transformed into the proposed smart loads.**

***Index Terms*—demand response, electric spring, frequency control, microgrid, smart load, virtual inertia.**

I. Introduction

TRADITIONAL power systems comprise multiple synchronous generators with large rotational inertia which can absorb or release energy for maintaining system frequency stability [1]. For emerging power systems with high penetration of renewable energy resources such as wind turbines and solar photovoltaic (PV) arrays, the power converter interfaces of the renewable energy sources usually operate with maximum power point tracking (MPPT) without providing much inertia or frequency support. Thus, higher renewable penetration may lead to lower equivalent system inertia in the power grid. As the primary frequency control, which is in the time-scale of seconds, is contributed by both frequency droop and inertia [2], the reduction of inertia in future power system with higher renewable penetration challenges the power grid frequency stability. During a frequency event, the frequency nadir and especially the rate of change of frequency (RoCoF) are closely related to the system inertia. It has been reported that pole slipping could occur when the RoCoF ranges from 1.5 Hz/s to 2 Hz/s [3], by which the protective tripping of generating units and further the cascading outages may happen. So inertia enhancement is needed to avoid excessive RoCoF and mitigate the frequency fluctuation in future power network with high renewables and low inertia.

A recent review of inertia of future more-electronics power systems [4] has identified (i) synchronous condensers, (ii) wind turbines, (iii) DC-link capacitors, (iv) ultra-capacitors, (v) batteries and (vi) virtual synchronous machines (VSMs) as inertia enhancement techniques [4]. Among these inertia enhancement techniques, a simple solution is to add more backup synchronous generators with partial loading for spinning reserve or even synchronous condensers to provide more rotating masses [4]. But it undoubtedly leads to higher capital investment and operating cost. The idea of inertia emulation by wind turbines is proposed in [5] and further analyzed in [6, 7]. By adding frequency response capabilities in the wind turbines, the inertial response can be obtained from the kinetic energy stored in the wind turbines. Recently, provision of distributed virtual inertia through general grid-connected converters by allowing the dc-link voltage of the converters to fluctuate within the permissible range has been proposed [8][15]. This is achieved by simply linking the dc voltage reference with the system frequency. Another well-known technology that can provide synthetic inertia is virtual synchronous generators (VSGs) [9] or virtual synchronous machines (VSMs) [10]. Strategies to control the grid-connected inverter to operate like a synchronous generator has been introduced in [11]. Although one can assign and change the virtual inertia value of the VSG by modifying the control parameters [12], large power rating of the power converter and additional energy storage units are needed accordingly.

The inertia techniques reviewed in [4] focus primarily on the power supply side and energy storage devices. The novel contribution of this paper is to explore the inertia emulation potential from the load side based on electric spring technology. In existing literature, the use of electric vehicles [13] and thermal loads [14] for providing frequency support to the power grid has been reported. In [15], a smart lighting system is designed to enable automatic demand response. Other literature also investigates the optimal load modulation method [16, 17] on how to adjust controllable loads in the power system to rebalance power and regulate the system frequency while minimizing the aggregated disutility of controllable loads.

In this paper, the electric spring (ES) technology is used to control the ac mains voltage within its specified tolerance (e.g. +/-5%) so that all voltage-dependent loads can be modified into smart loads (SL) with adaptive power consumption [18]. It is revealed in [19] that the "active power reserve", which is stored in general loads because of the allowable ±5% nominal load voltages variation, is significant and can be utilized to offer some ancillary services to the power system. In this paper, the "active power reserve in general loads" by using ES to modulate the load voltage within the range of 0.95~1.05 times of the nominal ac mains voltage value is investigated from a virtual inertia point of view. The control scheme for the ES-based SL is designed for providing equivalent load-side virtual inertia and primary frequency response at the same time.

The paper is organized as follows: A general review of popular supply-side virtual inertia methods and a preview of the proposed smart load method are given in Section II. The

detailed design of electric-spring-based smart load is introduced in Section III. In Section IV, the equivalent virtual inertia and load damping effects and the corresponding inertia coefficient H_{SL} and load damping coefficient D_{SL} are derived and verified by a "mini-grid" simulation. Finally, a case study based on the CIGRE microgrid benchmark is included to demonstrate how much system inertia can be increased during the day by turning all the domestic loads in that grid into the proposed smart loads.

II. Supply-side and Load-side Virtual Inertia

A. *Supply-side Virtual Inertia Technologies*

In this section, some mainstream supply-side virtual inertia technologies with or without the energy storage are briefly discussed. Renewable energy sources (RESs) that are interfaced to the power grid through power converters do not inherently contribute to system inertia. However, it is well known that the power control loop of the converters can be modified to make the RESs contribute 'virtual' inertia without the need for any energy storage. Several utilities (e.g. Hydro Quebec [23]) require the wind turbine generators to provide inertial response by reducing the turbine speed to release the stored kinetic energy. Although there is significant amount of kinetic energy stored in wind turbines [24][25], their virtual inertia contribution is limited by several factors such as the recovery phase (depending on the prevailing wind speed) to regain the turbine speed, the rated capacity of the grid interface power converters and the mechanical stress on the turbine components and the associated impact on lifetime.

For solar photovoltaic (PV), virtual inertia can be provided by operating below maximum available power (i.e. part-rated operation) [26] to keep a margin for increasing the power output when required. The economic implication of such part-rated operation needs to be carefully considered against alternative sources of virtual inertia [27]. This is where smart loads could complement the existing solutions as an additional source of virtual inertia.

When there is energy storage in the dc-link of converter-connected energy sources, virtual synchronous generator (VSG) [20] technology can be adopted. Fig.1 shows a DES connected to the power grid by using VSG technology. The renewable energy sources (like wind turbines or solar panels) are connected to the dc-link by using some resource-side-converter (RSC). The RSC is controlled by maximum-power-point-tracking (MPPT) algorithm. It is shown in Fig.1 that the VSG output voltage amplitude reference is generated by a reactive power control loop while the VSG output voltage frequency reference is generated by an active power control loop. The governor and swing equation characteristics are emulated in the active power control loop of VSG. (Readers are advised to refer to [20] for the details of VSG control.) In VSG, the inertia coefficient H_{VSG}, load damping coefficient D_{VSG} and droop coefficient R_{VSG} can be defined and modified by the users. However, the possible inequality of input and output power of the converters under VSG control is an issue. Since the power converters are incapable of handling the power imbalance by absorbing/delivering kinetic energy like true generators, energy storage system such as batteries is always needed to achieve the power management in VSG [21]. In [22], the power balance of the wind turbine VSG system and the sizing design of the batteries have been addressed.

Using the variable dc-link voltage method to exploit the energy reserved in the dc-link capacitors of grid-side-converter (GSC) for virtual inertia emulation is extensively reported recently [8][15]. An illustration of the implementation of both modified RESs and variable dc-link voltage together without energy storage in the dc link is shown in Fig.2. The GSC is controlled to regulate the dc-link voltage to the given reference value. (For permanent magnet synchronous generator (PMSG)- and doubly-fed induction generators (DFIGs) based wind turbine systems, GSC is an ac-ac inverter; for solar power system, GSC is a dc-dc converter.)

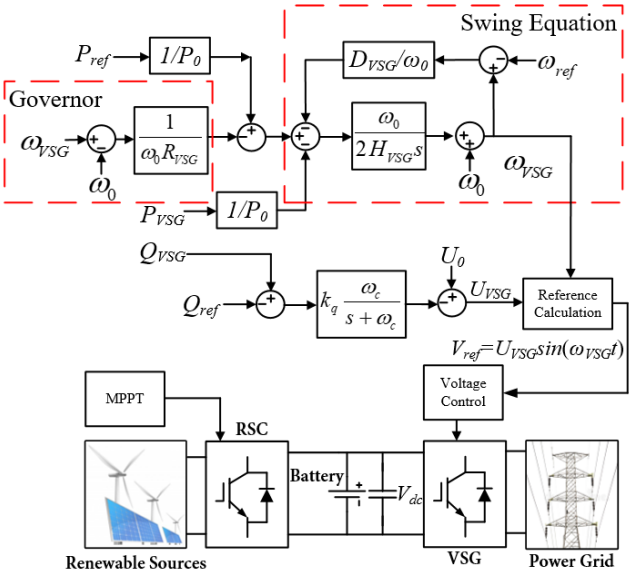

Fig.1 VSG control scheme

The proportional gain K_C in Fig.2 is defined as [8]:

$$K_C=\left(\frac{\Delta V_{dc-\max}}{V_{dc}}\right)/\left(\frac{\Delta f_{\max}}{f_{ref}}\right) \tag{1}$$

where V_{dc} and f_{ref} are the nominal dc-voltage and frequency; $\Delta V_{dc\text{-}max}$ and Δf_{max} are the maximum allowable voltage fluctuation and frequency deviation. In this case, the virtual inertia coefficient is [8]:

$$H_C=K_C\cdot\frac{C_{dc}V_{dc}^2}{2S_0} \tag{2}$$

where C_{dc} and S_0 are the dc capacitance and power rating of the grid-side-converter, respectively.

It can be observed in (2) that the virtual inertia emulated is related to the dc-capacitance and K_c. Considering the dc-capacitor is always designed to be as small as possible by the manufacturer to save cost and the value of K_c is somewhat restricted by the allowable dc-voltage deviation, the feasible value of H_c is rather limited in the real application unless larger capacitor or super-capacitor is used. It is reported in [28] that 17 times of the normal HVDC link capacitance is needed if one

wants to achieve a considerable virtual inertial coefficient of H=2.5s by allowing 10% dc voltage deviation [28] in a HVDC-link for an offshore wind farm. Similarly, drawbacks also exist for modified RESs.

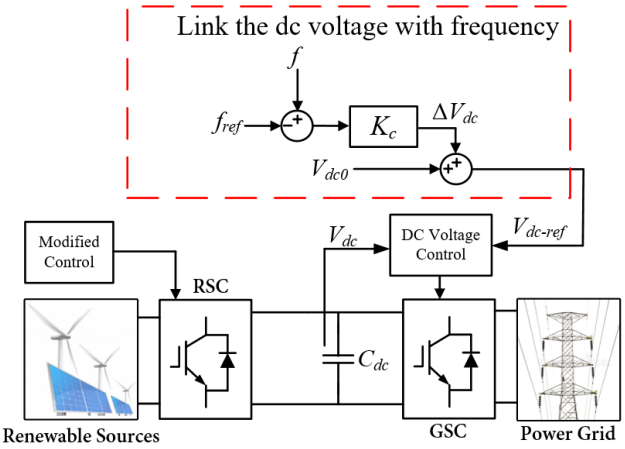

Fig.2 Virtual inertia technology without BSS

B. Load-side Virtual Inertia from Smart Loads

Unlike the aforementioned methods of obtaining virtual inertia on the supply-side (i.e. within the DES), this study aims at studying virtual inertia on the load-side. Electric spring is an emerging smart load technology suitable for fast demand-side response. The effectiveness of electric-spring-based smart loads (ESB-SL) for voltage regulation [29] [30], primary frequency control [31], overvoltage prevention [32], power quality improvement [33], power system restoration [34] has been demonstrated previously. It is the first time, in this paper, that the virtual inertia function of the ESB-SL is explored and the inertia enhancement is quantified.

Voltage-dependent loads (i.e. not confined to electric vehicles, thermal loads or lighting loads) can be transformed into smart loads when combined with the ES-B2B [35]. Fig.3 shows the single-phase equivalent of the proposed smart load. The ES-B2B consists of a shunt inverter and a series inverter [35]. In this paper, the smart load is proposed for creating equivalent virtual inertia (H_{SL}) and providing primary load frequency response while the load voltage of the load connected to ES-B2B (V_L) is kept within the permissible range of ±5% of the nominal load voltage. The detailed control scheme and principles are demonstrated in Section III.

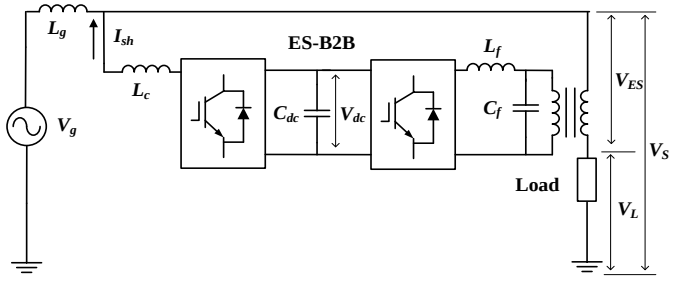

Fig.3 Single-phase equivalent of a smart load

Assuming in a power system with (*a*) traditional synchronous generators, (*b*) DESs and (*c*) loads, (*d*) loads are transformed into smart loads. In a power grid, the supply-demand relationship should be:

$$\sum_{i=1}^{a} S_{Gi} + \sum_{i=1}^{b} S_{DESi} \geq \sum_{i=1}^{d} S_{SLi} + \sum_{i=1}^{c-d} S_{RLi} \tag{3}$$

where S_{Gi}, S_{DESi}, S_{SLi} and S_{RLi} are the power ratings of the synchronous generators, DES, smart loads and remaining loads.

Since the inertia coefficient of the synchronous generators (H_{Gi}), virtual inertia coefficient of DES (H_{DESi}) and (H_{SLi}) are all defined based on their respective power ratings, the overall combined system inertia can be deduced as:

$$H_{sys} = \frac{\sum_{i=1}^{a} S_{Gi} \cdot H_{Gi} + \sum_{i=1}^{b} S_{DESi} \cdot H_{DESi}}{\sum_{i=1}^{a} S_G + \sum_{i=1}^{b} S_{DES}} + \frac{\sum_{i=1}^{d} S_{SLi} \cdot H_{SLi}}{\sum_{i=1}^{a} S_G + \sum_{i=1}^{b} S_{DES}} \tag{4}$$

It can be seen in (4) that the system inertia can be improved from both the supply-side (H_{DESi}) and load-side (H_{SLi}). The virtual inertia from supply-side will be "diluted" by the penetration rate of the DES without virtual inertia features. The last term of (4) involves the power of smart loads. It shows that the load-side virtual inertia is an alternative solution to complement existing supply-side solutions to increase the system inertia.

III. Electric Spring and Smart Load

The control scheme of the electric-spring-based smart load is shown in Fig.4. The three-phase ES-B2B is controlled in the d-q rotating reference frame. The power invariant park- and inverse-park- transformations are used to transform the measured voltages and currents into rotating coordinates for control purpose. The local bus voltage phase and frequency measurement are based on the SRF-PLL [36] and the RoCoF is obtained by a differential operator. The dynamics and stability issues of using derivative technique for inertia emulation are discussed in [37]. Note that the PLL may shape the impedance of power converters into a negative resistance in the quadrature-axis (q-axis) [38] and thus result in low frequency oscillation, so the PLL parameters need to be carefully designed as explained in [39].

The series inverter's output voltage V_{ES} (also known as ES output voltage) is controlled to be in-phase or out-of-phase with the local bus voltage in order to modulate the load voltage within the +/-5% tolerance and thus change the smart load power consumption (so $V_{ESq\text{-}ref}$=0, V_{ES}= V_{ESd} in the steady-state). In order to provide distributed virtual inertia and load response:

$$V_{ESd-ref} = y = \frac{V_0}{f_0}(K_1 \Delta f + K_2 \cdot RoCoF) \tag{5}$$

$$V_{ESd-ref} = \begin{cases} (V_S - 0.95V_0), \text{if } (V_S - 0.95V_0) < y \\ y, \text{if } (V_S - 1.05V_0) < y < (V_S - 0.95V_0) \\ (V_S - 1.05V_0), \text{if } y < (V_S - 1.05V_0) \end{cases} \tag{6}$$

The conditional equation (6) involves a dynamic saturation limit (related to the measured local bus voltage V_S and nominal bus voltage V_0) to limit the ES output voltage to ensure the

voltage of the load connected to ES-B2B is kept within the range of ±5% of the nominal voltage. It will be shown in Section IV that the derivative gain (K_2) and the proportional gain (K_1) are closely related to the equivalent virtual inertial factor and load damping factor.

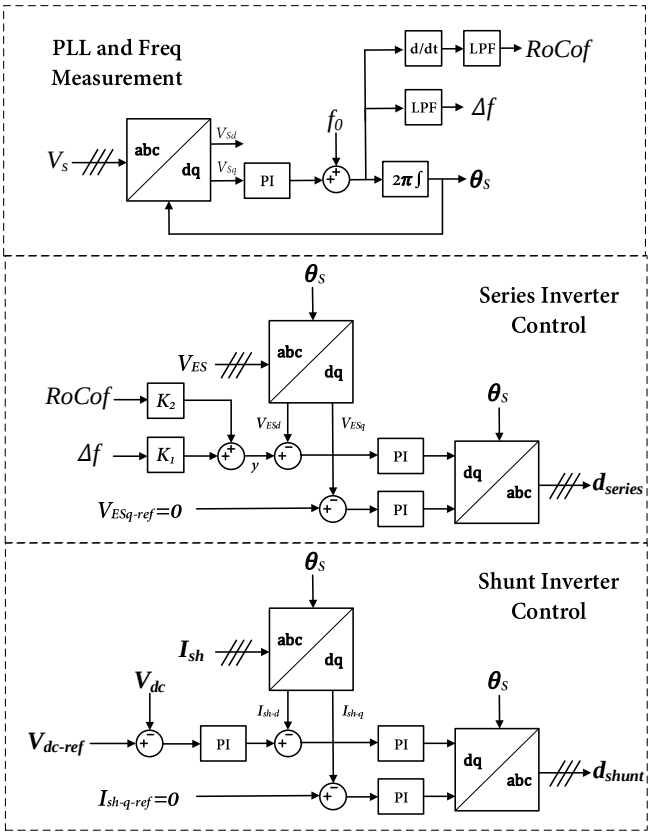

Fig.4 Control scheme of ES-B2B

The shunt inverter, on the other hand, is used to maintain the dc-link voltage. It is a current-controlled-inverter operated in unit-power-factor mode (i.e. $I_{shq\text{-}ref}$ =0). The voltage phasor diagrams and the power flow diagrams when the ES output voltage (V_{ES}) is in phase and out of phase with the local bus voltage (V_S) are shown in Fig.5(a) and Fig.5(b) respectively. In Fig.5, P_{SL}, P_L, Q_{SL} and Q_L are the active and reactive power consumption of the smart load and the load connected to the ES-B2B. And P_{ES} and Q_{ES} are the active and reactive power flow through the series inverter of ES-B2B, respectively. It is shown in Fig.5 that the active power absorbed/released by the series inverter (P_{ES}) is either fed into/drawn from the grid by the shunt inverter. So actually, P_{SL}=P_L. By using the exponential load model [1] for the general load connected to the ES-B2B:

$$P_{SL} = P_L = P_0\left((V_S - V_{ES})/V_0\right)^{n_p} \tag{7}$$

$$S_{ES} = \frac{S_L}{V_L}V_{ES} = \sqrt{P_0^2\left(\frac{V_L}{V_0}\right)^{2n_p} + Q_0^2\left(\frac{V_L}{V_0}\right)^{2n_q}}\,\frac{V_{ES}}{V_L} \tag{8}$$

where P_0, Q_0, S_0 and V_0 are the nominal active power, nominal reactive power, nominal apparent power and nominal voltage of the load connected to ES-B2B2 respectively; n_p and n_q are the active and reactive power sensitivity of that load. ($0 \le n_p, n_q \le 2$).

The two inverters of the ES-B2B are designed to be with the same power rating in this paper. When n_p=n_q=2, V_L=1.05V_0, V_S=0.95V_0, V_{ES}=-0.1V_0, the apparent power flow through the series inverter of ES-B2B (S_{ES}) reaches its maximum value of 0.105S_0 according to (8). Given some margin, the power rating of the two inverters of the ES-B2B should be designed to be 0.15S_0 each. It should be noted that a majority part of the power utilized to provide inertia support comes from the change of load consumption. Extra power loss of this method comes from switching and conduction loss of the power converter, which is small and negligible compared with the load consumption.

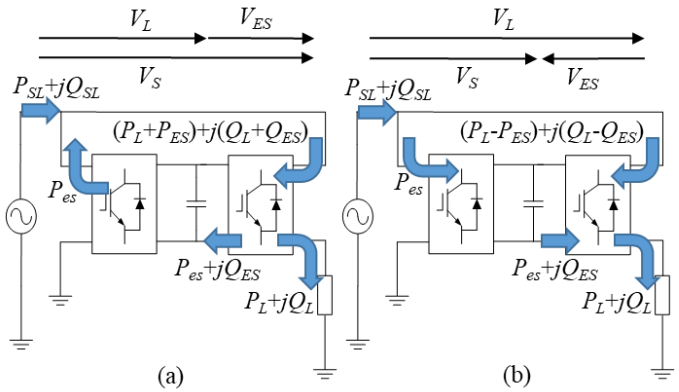

Fig.5 Voltage phasor diagrams and the power flow situation

The circuit parameters and specifications of a 10kW, 1kVar sample electric-spring-based smart load are listed in TABLE I.

There are three closed control loops in the smart load:

1) the ac current control loop of shunt inverter
2) the dc-link voltage control loop of the shunt inverter
3) the ac voltage control loop of the series inverter.

The controller parameters of these three control loops are chosen in this section by assigning reasonable bandwidths. The control parameters of the three control loop of the sample electric-spring-based smart load are selected following the guideline in [40] (i.e. assign the bandwidth of inner loop control

TABLE I

SMART LOAD PARAMETERS AND SPECIFICATIONS

Symbol	Quantity	Value
V_0	Nominal Line to line RMS voltage	380V
f_0	Nominal system frequency	50Hz
P_0	Nominal load active power	10kW
Q_0	Nominal load reactive power	1kVar
n_p	Load active power-voltage sensitivity	2
n_q	Load reactive power-voltage sensitivity	2
V_{dc}	DC-link voltage	700V
L_c	Shunt inverter filter inductor	5mH
L_f	Series inverter filter inductor	5mH
C_f	Series inverter filter capacitor	10μF
C_{dc}	DC-link capacitor	1000μF
f_{sw}	Switching frequency	10kHz

to be $0.2f_{sw}$ and the bandwidth of dc voltage to be less than $0.02f_{sw}$) and are listed in TABLE II.

IV. Equivalent Virtual Inertia From Smart Load

TABLE II

CONTROL PARAMETERS OF ES-B2B

Symbol	Quantity	Value
K_{pac}	Proportional gain of ac current control	0.05
K_{iac}	Integral gain of ac current control	5
K_{pdc}	Proportional gain of dc voltage control	1
K_{idc}	Integral gain of dc voltage control	0.1
K_{pav}	Proportional gain of ac voltage control	0.01
K_{iav}	Integral gain of ac voltage control	0.2

A. Equivalent System Effect

In this section, the equivalent virtual inertia and load damping effect introduced by the smart load (based on the small-signal approximation and in the per-unit system) are analyzed. The base voltage and base power are equal to the nominal smart load line-to-line RMS voltage and nominal active power consumption (i.e. the smart load active power consumption when ES output voltage is zero.) respectively. And $\bar{x}$ represents variable x in the per-unit system.

The proposed approach is first discussed for an aggregated system based on an equivalent generator supplying a smart load as shown in Fig.6. For the "nano-grid" in Fig.6: S_G=S_{SL}. The frequency response block diagram for the generator is based on that in [1]. The bandwidth of the SRF-PLL is chosen as 10Hz which is enough to capture the system frequency fluctuation [40]. The time constant of the low pass filter (LPF) of frequency and RoCoF detection is chosen to be as small as 0.01s (so that the influence of the delay effect of LPF to the system frequency response is negligible).

Incremental changes in load voltage and power consumption can be expressed as (ω is the angular velocity):

$$\Delta V_L = -V_{es} = \frac{V_0}{\omega_0}(K_1\Delta\omega + K_2\frac{d\omega}{dt}) \tag{9}$$

$$\Delta P_{SL} = n_p P_0 (\frac{V_L}{V_0})^{n_p}\frac{\Delta V_L}{V_L} \tag{10}$$

TABLE III

PARAMETERS OF THE EQUIVALENT GENERATOR SUPPLYING THE SMART LOAD

Symbol	Quantity	Value
P_0	Nominal active power reference	10kW(1p.u.)
R	Droop coefficient	0.05
F_{HP}	Turbine HP coefficient	1 s
T_{RH}	Time constant of reheater	0.1 s
T_{CH}	Time constant of main inlet volumes	0.01s
H	Inertia coefficient	5 s
D	Original load damping coefficient	0
Δf_{max}	Maximum allowable frequency deviation	0.8 Hz
$RoCoF_{max}$	Maximum allowable frequency rate of change	1 Hz/s
K_1	Proportional gain of smart load	3.125
K_2	Derivative gain of smart load	2.5

The proportional (K_1) and derivative gain (K_2) of smart load are chosen as:

$$K_1 = \frac{\Delta V_{\max}}{V_0}\frac{f_0}{\Delta f_{\max}} = \frac{\Delta V_{\max}}{V_0}\frac{\omega_0}{\Delta\omega_{\max}} \tag{11}$$

$$K_2 = \frac{\Delta V_{\max}}{V_0}\frac{f_0}{(df/dt)_{\max}} = \frac{\Delta V_{\max}}{V_0}\frac{\omega_0}{(d\omega/dt)_{\max}} \tag{12}$$

where the ΔV_{max}, Δf_{max} and $(df/dt)_{max}$ are the maximum allowable load voltage variation, system frequency and frequency change respectively. The control gains are designed according to the U.K. National Grid requirement (Δf_{max}=0.8Hz [41] and $(df/dt)_{max}$=1Hz/s [42]). In this study, $\Delta V_{max}/V_0$ is set at 5%. So the K_1 and K_2 values are calculated by (11) and (12) and they are listed in TABLE III.

According to the kinetic theory of the generator (J is the rotational inertia of the generator) [1]:

$$\Delta P_m - \Delta P_{SL} = J\omega\frac{d\omega}{dt} \tag{13}$$

From (10) and (13), one can get (14) in the per-unit system: (the delay effect of the low pass filter is negligible with respect to the relatively slow variation in frequency)

$$\Delta\bar{P}_m - (\frac{V_L}{V_0})^{n_p-1} n_p K_1 \Delta\bar{\omega} = (2H + (\frac{V_L}{V_0})^{n_p-1} n_p K_2)\frac{d\bar{\omega}}{dt} \tag{14}$$

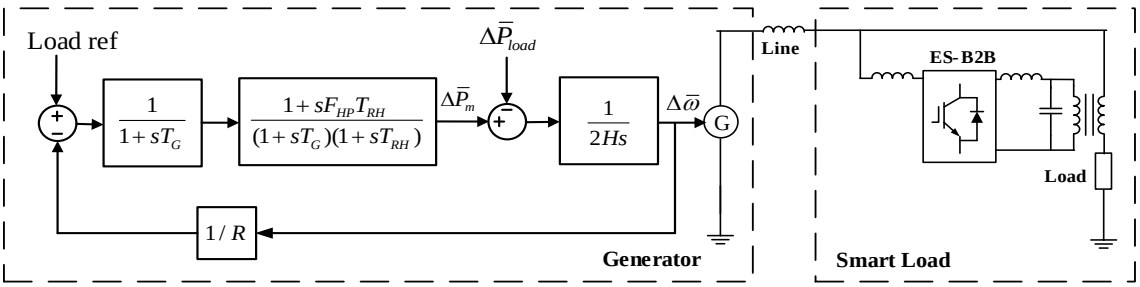

Fig.6 Block diagram of an equivalent generator supplying a smart load

$$H = J\omega^2 / 2P_0 \tag{15}$$

The relationship between the frequency and power fluctuations can be expressed as:

$$\frac{\Delta\bar{\omega}}{\Delta\bar{P}_m} = \frac{1}{2(H + (\frac{V_L}{V_0})^{n_p-1}\frac{n_pK_2}{2})s + (\frac{V_L}{V_0})^{n_p-1}n_pK_1} = \frac{1}{2(H+H_{SL})s + D_{SL}} \tag{16}$$

The equivalent block diagram of the system frequency response is shown in Fig.7. From (16) and Fig.7, it is found that the smart load actually adds two terms in the frequency response block diagram, one is the virtual inertia term H_{SL} and the another is the smart load damping term D_{SL}. Assuming the allowable load voltage variation to be ±5% and take an approximation of $V_L/V_0 \approx 1$, roughly we have:

$$H_{SL} = n_pK_2 / 2 \tag{17}$$

$$D_{SL} = n_pK_1 \tag{18}$$

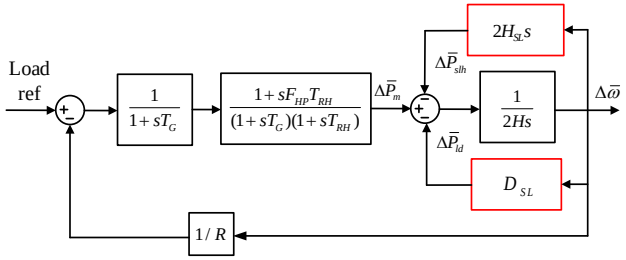

Fig.7 Block diagram of system frequency with equivalent effect of the smart load

Given n_p ranks from 0 to 2, the inertia H_{SL} of the smart load could be at most around 2.5s (when n_p=2) based on its power rating according to (17).

B. *Simulation Verification*

The dynamic response of the above system is simulated by inserting an additional 2000W resistive load in parallel with the smart load (i.e. a load increase of 20%) at t= 2.0s. The circuit and control parameters are listed in TABLE I, II, III. Fig.8 shows the ES output voltage and dc-link voltage waveforms under this test condition. During the sharp rise of ES output voltage, the dc-link voltage shown in Fig.8(b) is tightly regulated to be around 700V. So the effectiveness of the chosen controller parameters in TABLE II is verified. Fig.9 shows the system's RoCoF and ES output voltage profiles with and without the derivative term in the smart load (i.e. without derivative term means K_2=0). With the derivative term, it is shown in Fig.9(b) that ES output voltage rises sharply in response to the load step change in the initial stage, which decreases the system maximum RoCoF from 1Hz/s (without the derivative term) to 0.6 Hz/s as shown in Fig.9(a). This effect is due to the virtual inertia provided by the smart load.

The dynamic excursion of the system frequency with various sets of parameters under the same load change are displayed in Fig.10. The first three traces show the system frequency responses with different D and H values of the generator and the smart load is not activated during the load step change process. (Blue trace: 2H=10 s, D=0; red trace: 2H=10 s, D=6.25; yellow trace: 2H=15 s, D=6.25.) The other two traces are with ES-B2B activated with different K_2 values and with D=0, 2H=10s applied to the generator. It is clear from Fig.10 that the trace with triangle markers closely matches with the red trace, which indicates that the equivalent system effect of the smart load with K_1=3.125 and K_2=0 is increasing D from 0 to 2×3.125=6.25. Similarly, since the trace with star markers closely matches with the yellow trace, the equivalent system effect of smart load with K_2=2.5 is increasing $2H$ from 10s to 10s+2×2.5s=15s. The simulation results corroborate the theoretical estimations based on (17) and (18).

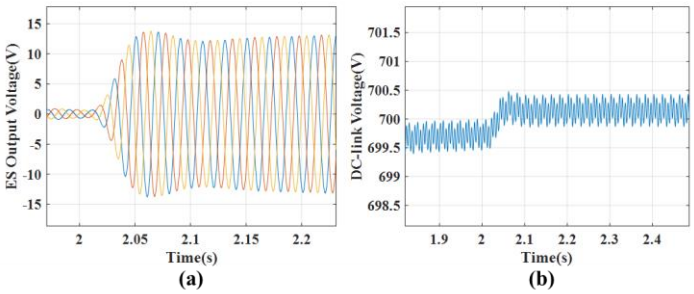

Fig.8 Voltage waveforms after the load step change (a) the ES output voltage (b) the dc-link voltage

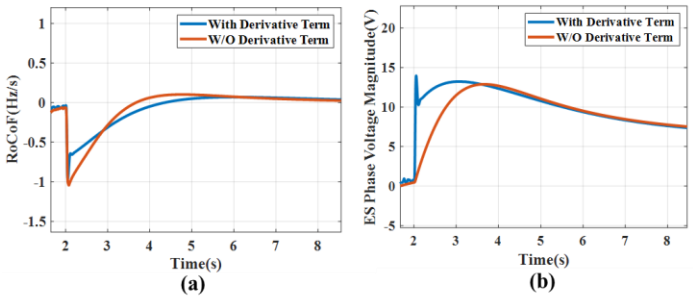

Fig.9 Simulation results (a) RoCoF (b) ES output phase voltage magnitude

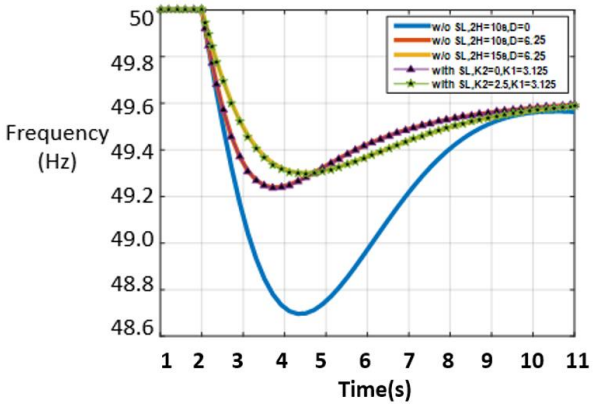

Fig.10 Frequency variation with 20% increase in load

V. Case Study in the CIGRE Microgrid

To further substantiate and evaluate the distributed inertia support from the smart loads (SLs), a case study is presented in this section using an isolated microgrid scenario with CIGRE European benchmark medium- and low-voltage (MV/LV) network [43], as shown in Fig.11. In the following subsections, the level of inertia contributed by the SLs for different time periods of the day is firstly presented. Then the results of a time-domain simulation are included to demonstrate the effectiveness of virtual inertia from the SLs.

A. System Description

The total diversified peak demand (DPD) of the system throughout a day is about 5.5 MVA, served by two diesel generators at bus 1 & 12 with a rated capacity of 3.125 MVA each and 1MW wind power generation connected at bus 7, operated under the maximum power point tracking mode with unity power factor at its point of coupling. The diesel generators are represented using a third-order dynamic model with the parameters provided in [44]. The IEEE-DC1A type excitation system and governor (using first-order model) with 5% power-frequency droop are used for both generators.

Domestic loads, which account for 70% of the total DPD, are all connected to LV level while the remaining are industrial/commercial loads, all connected directly at MV level. Each box marked with 'LV' in Fig.11 represents multiple CIGRE LV networks connected in parallel. The number of LV networks and the number of households aggregated at each node (R11, R15-R18) within an LV network is decided by their DPD respectively, as given in [43]. The domestic demand and power voltage sensitivity profiles are obtained in a bottom-up way from appliance level to a cluster of households level with 1-min resolution as expressed in [19]. Each cluster of households located at R11, R15-R18 of the CIGRE LV network is connected in series with an ES-B2B and is transformed into the smart load. There are 31 LV feeders and altogether 155 smart loads in the CIGRE system. The proportional gain (K_1) and derivative gain (K_2) of smart loads are the same as in Section IV.

B. Estimated Virtual Inertia from Smart Loads

The inertia contribution (H_{SL}) for each cluster of domestic customers can be estimated by using (16), for which the voltage profiles could be obtained through power flow results. Readers are advised to refer to [19] for load, power-voltage sensitivity (n_p) and voltage profiles for each cluster of domestic loads during winter and summer weekdays. The virtual inertia coefficient of smart loads are first calculated based on the load power rating as expressed in (19).

$$H_{SL} = \left(\sum_{i=1}^{d} S_{SLi} \cdot H_{SLi}\right) / \left(\sum_{i=1}^{d} S_{SLi}\right) \tag{19}$$

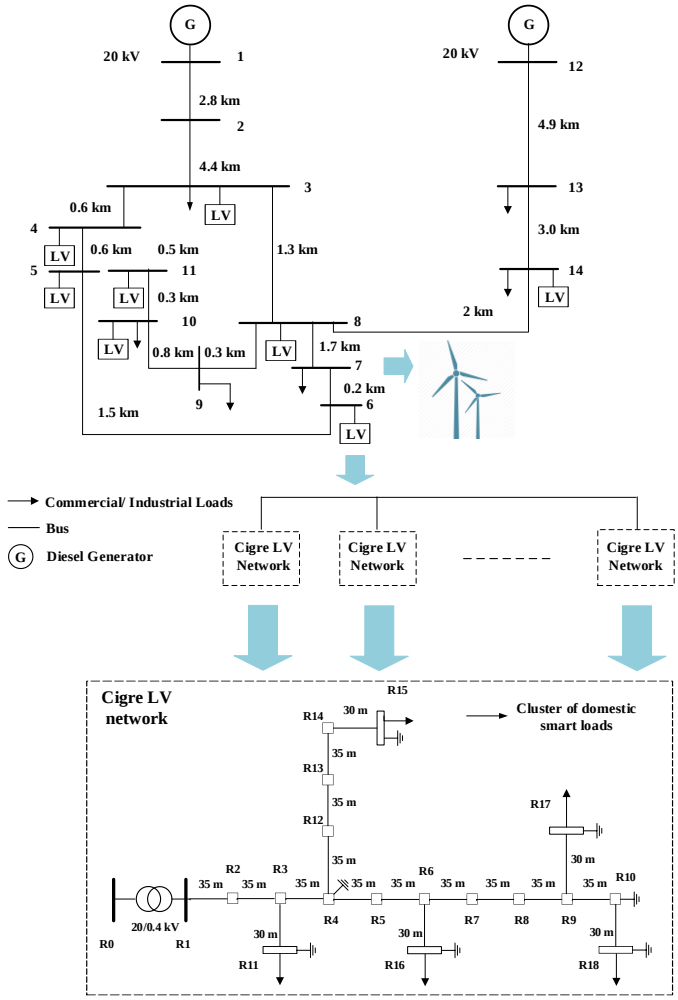

Fig.11. Isolated microgrid with CIGRE European benchmark network

The variations in inertia contribution by the domestic sector loads profiles considering several winter/summer weekdays are shown in Fig. 12. Three traces represent the upper boundary (95 pc), median value and lower boundary (5 pc) situation considering the different load consumption situations in different days. When K_2 is fixed, the variation of the total inertia in this case is determined by power-voltage sensitivity (n_p), voltage profiles and the ratio of domestic active power consumption. It can be seen that inertia value peaks during winter night hours due to the usage of electric heating while hits the bottom during similar sessions for summer when both the power consumption and power-voltage sensitivities for the domestic sector are low. It is shown in Fig.12 that for most time of the day, these smart loads can provide additional virtual inertia of around 1.3 s. It should be mentioned that the inertia provided from SLs is lower than expected due to the fact that active power-voltage sensitivities (n_p) of the domestic loads in the CIGRE network are mostly below 2 (ranging from 0.4 to 1.7).

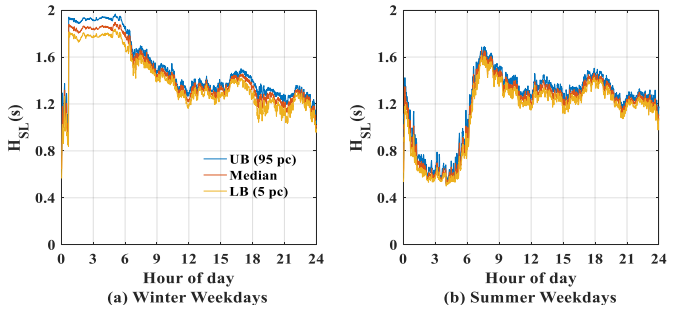

Fig. 12. Equivalent inertia for (a) winter weekdays and (b) summer weekdays

C. Time Domain Simulation Verification

At t=60s, 50% of the wind generation is suddenly disconnected to create a disturbance (Fig.13). The load demand and the power voltage sensitivity are based on the 7:30am data from winter weekdays and are assumed to be constant throughout the simulation. The frequency and load-side voltage response before and after the disturbance are given in Fig. 13. Compared to the case without any smart loads (blue curve in Fig.13(a)), it can be seen that the RoCoF and frequency nadir of the case with smart loads (red curve in Fig.13(a)) are both improved due to the smart loads with acceptable load voltages ($\geq$ 0.95 p.u.) as shown in Fig.13(b).

To quantify the equivalent system inertia enhancement acquired from the smart loads, a case using generators with additional inertia of ΔH_{sys}=0.53s and without using smart load is also provided in Fig.13(a) (marked in brown). It can be observed that during the dynamic process, the red trace (with smart loads) and brown trace (equivalent generator with increased inertia) coincide at the very beginning, which indicates that the equivalent system inertia enhancement from the smart loads at the initial stage is around 0.53s. It should be mentioned that this ΔH_{sys}=0.53s value is based on total generator rating (which is just like the last term of equation (4)). It would be around 1.4s if translating to the smart load power rating according to (19). This fitting result matches the estimation results in Section V part B that the H_{SL} will be around 1.3s during the day.

It should be noted that the equivalent system inertia increment of 1.4s is less than the estimated results as shown in Fig.12(a) at 7:30am (which is around 1.6s). This is due to some smart loads (not all) reaching their lower voltage limit of 0.95p.u. as shown in Fig.13 (b). This situation lasts for around 0.9s as can be seen in Fig.13 (b). Note that no inertia can be emulated from the smart load once its load voltage is fixed at 0.95p.u.. So during that 0.9s duration, the system total virtual inertia coefficient of the smart loads together is lower than the estimation outcome from (19) because some of the smart loads are saturated in voltage and loss their virtual inertia effect. In addition, it is observed that the grid frequency settles to the steady-state value faster with SLs (red trace) in Fig.13(a) compared to the case with "Equivalent Gen" (brown trace). The reason is that the virtual inertia contribution from the smart loads will recover to the estimated value once the load voltages are restored back within the voltage range. So the H_{SL} actually recovers back to be larger than 1.4s (Equivalent Gen case) after those situation disappears, thus making the frequency settle quicker to the steady-state value.

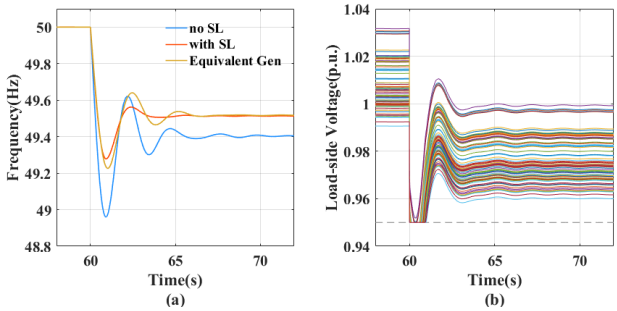

Fig. 13. Frequency and load-side voltage response before and after sudden disconnection of 50% of wind generation

Fig.14 shows what will happen if the proposed frequency response and virtual inertia service of electric springs are deactivated at t = 70s. The load voltages are restored to their original values after t = 70s. At the same time, the primary frequency regulation and inertia enhancement effect are lost, and the system frequency further dropped from around 49.5Hz to 49.4Hz. However, the system frequency nadir during the whole process improved from 48.95Hz to 49.3Hz. (Note that 48.95Hz is the frequency nadir for the situation without smart load as shown in Fig.13(a).). In addition, the deactivation of the frequency response and inertia emulation service leave space for the electric springs to achieve other services (such as voltage regulation [32], power quality improvement [33], etc.) as previously reported.

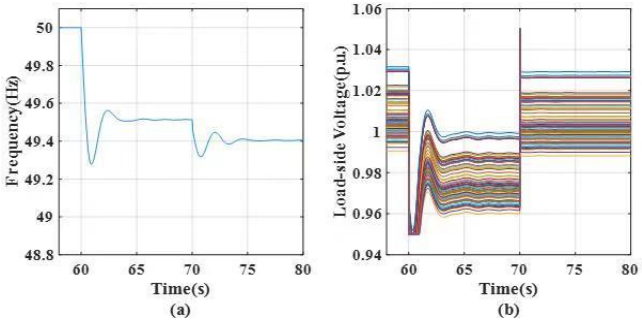

Fig. 14. Frequency and load-side voltage response after service deactivation.

VI. Conclusion

Unlike many previous studies of virtual inertia from the power supply side, this paper aims at evaluating and quantifying virtual inertia from the demand side by using electric spring technology within the acceptable +/-5% of the ac mains voltage tolerance. In this paper, the implementation of virtual inertia through ES based SLs is proposed and evaluated. The virtual inertia and load damping coefficients of our proposed smart load are derived. Under the control design following the U.K. National Grid frequency requirement, up to 2.5 s of virtual inertia can be obtained from an impedance-type smart load (n_p=2). Then a case study based on the CIGRE benchmark microgrid with high-resolution domestic demand model demonstrates that the SLs can provide around 1.3 s of

inertia (with respect to the smart load power rating) during most part of the day. The system equivalent inertia can be increased by ΔH_{sys}=0.53s if all the domestic sector loads in the CIGRE network are transformed to be smart loads. The promising results indicate that the virtual inertia from SLs can play a significant role in complementing the depleting inertial contribution from the supply side in future power grids.

REFERENCES

[1] P. Kundur, N. J. Balu, and M. G. Lauby, in *Power system stability and control*. McGraw-hill New York, 1994.

[2] Y. G. Rebours, D. S. Kirschen, M. Trotignon, and S. Rossignol, "A survey of frequency and voltage control ancillary services—Part I: Technical features," *IEEE Trans. Power Syst.*, vol. 22, no. 1, pp. 350-357, 2007.

[3] W. Uijlings, D. K. L. C. Street, and S. London, "An independent analysis on the ability of Generators to ride through Rate of Change of Frequency values up to 2Hz/s," London, Tech. Rep, Feb. 08, 2013.

[4] J. Fang, H. Li, Y. Tang, and F. Blaabjerg, "On the Inertia of Future More-Electronics Power Systems," *IEEE J. Emerg. Sel. Topics Power Electron*., 2018.

[5] J. Ekanayake and N. Jenkins, "Comparison of the response of doubly fed and fixed-speed induction generator wind turbines to changes in network frequency," *IEEE Trans. Energy Convers.*, vol. 19, no. 4, pp. 800-802, 2004.

[6] J. Morren, J. Pierik, and S. W. De Haan, "Inertial response of variable speed wind turbines," *Electric Power Syst. Res.*, vol. 76, no. 11, pp. 980-987, 2006.

[7] J. F. Conroy and R. Watson, "Frequency response capability of full converter wind turbine generators in comparison to conventional generation," *IEEE Trans. Power Syst.*, vol. 23, no. 2, pp. 649-656, 2008.

[8] J. Fang, H. Li, Y. Tang, and F. Blaabjerg, "Distributed power system virtual inertia implemented by grid-connected power converters," *IEEE Trans. Power Electron.*, vol. 33, no. 10, pp. 8488-8499, 2018.

[9] J. Driesen and K. Visscher, "Virtual synchronous generators," in *IEEE Power and Energy Society General Meeting-Conversion and Delivery of Electrical Energy*, 2008, pp. 1-3: IEEE.

[10] H.-P. Beck and R. Hesse, "Virtual synchronous machine," in *9th International Conference on Electrical Power Quality and Utilisation*, 2007, pp. 1-6: IEEE.

[11] Q.-C. Zhong and G. Weiss, "Synchronverters: Inverters that mimic synchronous generators," *IEEE Trans. Ind. Electron.*, vol. 58, no. 4, pp. 1259-1267, 2011.

[12] J. Alipoor, Y. Miura, and T. Ise, "Power system stabilization using virtual synchronous generator with alternating moment of inertia *IEEE J. Emerg. Sel. Topics Power Electron*., vol. 3, no. 2, pp. 451-458, 2015.

[13] K. Kaur, M. Singh, and N. Kumar, "Multiobjective Optimization for Frequency Support Using Electric Vehicles: An Aggregator-Based Hierarchical Control Mechanism," *IEEE Syst. J.*, vol. 13, no. 1, pp. 771-782, 2017.

[14] V. Trovato, I. M. Sanz, B. Chaudhuri, and G. Strbac, "Advanced control of thermostatic loads for rapid frequency response in Great Britain," *IEEE Trans. Power Syst.*, vol. 32, no. 3, pp. 2106-2117, 2016.

[15] S.Y.R. Hui and E. Waffenschmidt, "Power supply supporting virtual inertia for grid control (Micro-spring converter)", US Patent application number 16/071,665, Jan 20 2017.

[16] A. Delavari and I. Kamwa, "Improved optimal decentralized load modulation for power system primary frequency regulation," *IEEE Trans. Power Syst.*, vol. 33, no. 1, pp. 1013-1025, 2017.

[17] C. Zhao, U. Topcu, N. Li, and S. Low, "Design and stability of load-side primary frequency control in power systems," *IEEE Trans. Autom. Control.*, vol. 59, no. 5, pp. 1177-1189, 2014.

[18] S. Y. Hui, C. K. Lee, and F. F. Wu, "Electric springs—A new smart grid technology," *IEEE Trans. on Smart Grid*, vol. 3, no. 3, pp. 1552-1561, 2012.

[19] J. Guo, B. Chaudhuri, and S. Y. R. Hui, "Flexible Demand through Point-of-load Voltage Control in Domestic Sector," *IEEE Trans. on Smart Grid*, 2018.

[20] X. Meng, J. Liu, and Z. Liu, "A Generalized Droop Control for Grid-Supporting Inverter Based on Comparison Between Traditional Droop Control and Virtual Synchronous Generator Control," *IEEE Trans. Power Electron.*, vol. 34, no. 6, pp. 5416-5438, 2018.

[21] J. Fang, Y. Tang, H. Li, and X. Li, "A battery/ultracapacitor hybrid energy storage system for implementing the power management of virtual synchronous generators," *IEEE Trans. Power Electron.*, vol. 33, no. 4, pp. 2820-2824, 2017.

[22] Y. Ma, W. Cao, L. Yang, F. F. Wang, and L. M. Tolbert, "Virtual synchronous generator control of full converter wind turbines with short-term energy storage," *IEEE Trans. Ind. Electron.*, vol. 64, no. 11, pp. 8821-8831, 2017.

[23] J. Brisebois and N. Aubut, "Wind farm inertia emulation to fulfill Hydro-Québec's specific need," in *Proc. IEEE Power Energy Soc. Gen. Meeting*, 2011, pp. 1–7.

[24] F. Blaabjerg and K. Ma, "Future on power electronics for wind turbine systems," *IEEE J. Emerg. Sel. Topics Power Electron.*, vol. 1, no. 3, pp. 139–152, Sep. 2013.

[25] G. Lalor, A. Mullane, and M. O'Malley, "Frequency control and wind turbine technologies," *IEEE Trans. Power Syst.*, vol. 20, no. 4, pp. 1905–1913, Nov. 2005.

[26] A. F. Hoke, M. Shirazi, S. Chakraborty, E. Muljadi, and D. Maksimovic, "Rapid active power control of photovoltaic systems for grid frequency support," *IEEE J. Emerg. Sel. Topics Power Electron.*, vol. 5, no. 3, pp. 1154–1163, Sep. 2017.

[27] P. P. Zarina, S. Mishra, and P. C. Sekhar, "Deriving inertial response from a non-inertial PV system for frequency regulation," in *Proc. IEEE PEDES*, Bengaluru, India, Dec. 2012, pp. 1–5.

[28] A. Junyent-Ferr, Y. Pipelzadeh, and T. C. Green, "Blending HVDC-link energy storage and offshore wind turbine inertia for fast frequency response," *IEEE Trans. Sustain. Energy*, vol. 6, no. 3, pp. 1059-1066, 2015.

[29] S. Y. Hui, C. K. Lee and F. F. Wu, "Electric Springs—A New Smart Grid Technology," *IEEE Trans. on Smart Grid*, vol. 3, no. 3, pp. 1552-1561, Sept. 2012.

[30] T. Chen, H. Liu, C. Lee and S. Y. R. Hui, "A Generalized Controller for Electric-Spring-Based Smart Load with Active and Reactive Power Compensation," *IEEE J. Emerg. Sel. Topics Power Electron*., to be published. DOI: 10.1109/JESTPE.2019.2908730

[31] Z. Akhtar, B. Chaudhuri and S. Y. Ron Hui, "Primary Frequency Control Contribution From Smart Loads Using Reactive Compensation," *IEEE Trans. on Smart Grid*, vol. 6, no. 5, pp. 2356-2365, Sept. 2015.

[32] T. Chen, Y. Zheng, B. Chaudhuri and S. Y. R. Hui, "Distributed Electric-spring-based Smart Thermal Loads for Overvoltage Prevention in LV Distributed Network Using Dynamic Consensus Approach," *IEEE Trans. Sustain. Energy*, to be published. DOI: 10.1109/TSTE.2019.2950421

[33] S. Yan, S. Tan, C. Lee, B. Chaudhuri and S. Y. R. Hui, "Use of Smart Loads for Power Quality Improvement," *IEEE J. Emerg. Sel. Topics Power Electron*., vol. 5, no. 1, pp. 504-512, March 2017.

[34] L. Liang, Y. Hou, D. J. Hill and S. Y. R. Hui, "Enhancing Resilience of Microgrids With Electric Springs," *IEEE Trans. on Smart Grid*, vol. 9, no. 3, pp. 2235-2247, May 2018.

[35] S. Yan et al., "Extending the Operating Range of Electric Spring Using Back-To-Back Converter: Hardware Implementation and Control," *IEEE Trans. Power Electron.*, vol. 32, no. 7, pp. 5171-5179, 2017.

[36] L. N. Arruda, S. M. Silva, and B. Filho, "PLL structures for utility connected systems," in *Conference Record of the IEEE Industry Applications Conference*, 2001, vol. 4, pp. 2655-2660.

[37] E. Rakhshani and P. Rodriguez, "Inertia Emulation in AC/DC Interconnected Power Systems Using Derivative Technique Considering Frequency Measurement Effects," *IEEE Trans. Power Syst.*, vol. 32, no. 5, pp. 3338-3351, Sept. 2017.

[38] J. Fang, X. Li, H. Li and Y. Tang, "Stability Improvement for Three-Phase Grid-Connected Converters Through Impedance Reshaping in Quadrature-Axis," *IEEE Trans. Power Electron.*, vol. 33, no. 10, pp. 8365-8375, Oct. 2018.

[39] T. Kerdphol, F. S. Rahman, M. Watanabe and Y. Mitani, "Robust Virtual Inertia Control of a Low Inertia Microgrid Considering Frequency Measurement Effects," *IEEE Access*, vol. 7, pp. 57550-57560, 2019.

[40] L. Harnefors, M. Bongiorno, and S. Lundberg, "Input-admittance calculation and shaping for controlled voltage-source converters," ," *IEEE Trans. Ind. Electron.*, vol. 54, no. 6, pp. 3323-3334, 2007.

[41] National Grid.NETS Security and Quality of Supply Standard [Online]. Available: https://www.nationalgrideso.com/codes/security-and-quality-supply-standards

[42] Changes to the Distribution Code and Engineering Recommendation G59: Generator Connection Requirements [Online]. Available: https://www.ofgem.gov.uk/publications-and-updates/changes-distribution-code-and-engineering-recommendation-g59-generator-connection-requirements-review-engineering-recommendation-g59-3-1
[43] S. Barsali, Benchmark systems for network integration of renewable and distributed energy resources. 2014.
[44] K. Y. Yeager and J. Willis, "Modeling of emergency diesel generators in an 800 megawatt nuclear power plant," *IEEE Trans. Energy Convers.*, vol. 8, no. 3, pp. 433-441, 1993.

Tong Chen (S'17) received the B.S. degree in electrical engineering from Xi'an Jiaotong University, Xi'an, China, in 2016. He is currently working toward the Ph.D. degree in electrical and electronics engineering with the University of Hong Kong, Hong Kong, China. He was a exchange Ph.D. student with Imperial College London, London, U.K in 2019. His research interests include the stability and application of power electronics in power system and smart grid technology.

Jinrui Guo (S'16) received the B.Sc. and M.Sc. degrees from North China Electric Power University, Beijing, China, in 2012 and 2015, respectively. He is currently pursuing the Ph.D. degree from Imperial College London, U.K. His research interests include power system stability, smart grid, and renewable energy.

Balarko Chaudhuri (M'06–SM'11) received the Ph.D. degree in Electrical and Electronic engineering from Imperial College London, London, U.K., in 2005 where he is presently a Reader in Power Systems. His research interest includes power systems dynamics and stability, grid integration of renewable energy, wide-area control through HVDC/FACTS and demand response. Dr Chaudhuri serves as an editor of the IEEE Transactions on Smart Grid and an associate editor of the IEEE Systems Journal and Elsevier Control Engineering Practice. He is a Fellow of the Institution of Engineering and Technology (IET).

S. Y. (Ron) Hui (M'87-SM'94-F'03) received his BSc (Eng) Hons in Electrical and Electronic Engineering at the University of Birmingham in 1984 and a D.I.C. and PhD in Electrical Engineering at Imperial College London in 1987. Presently, he is a Chair Professor at the University of Hong Kong and Imperial College London. He received the IET Achievement Medal (The Crompton Medal) in 2010 and IEEE William E. Newell Power Electronics Award in 2015. He is a Fellow of the Australian Academy of Technological Sciences & Engineering (since 2010), US Academy of Inventors (since 2018) and the Royal Academy of Engineering, U.K. (since 2016).